Cao *et al. BMC Mat* (2020) 2:4
https://doi.org/10.1186/s42833-020-0010-6

BMC Materials

RESEARCH ARTICLE Open Access

Electron-transport properties of degenerate $ZnSnN_2$ doped with oxygen

Xiang Cao[1], Fumio Kawamura[2], Takashi Taniguchi[2] and Naoomi Yamada[1*]

Abstract

In this study, analysis of the electron mobility in $ZnSnN_2$ epilayers that were unintentionally doped with oxygen ($ZnSnN_{2-x}O_x$) was performed to elucidate the reason for the low mobilities of ~ 20 $cm^2 V^{-1} s^{-1}$. While roughly 30% of the incorporated oxygen donated electrons, the rest existed as neutral impurities. Seebeck-effect measurements revealed that scattering by neutral impurities governed the electron transport. The theoretical mobility calculated taking into account the scattering by neutral impurities and ionized impurities reproduced the experimental Hall mobility. We concluded that the low electron mobility is attributed to the presence of the neutral oxygen impurities in high concentration.

Keywords: $ZnSnN_2$, Mobility, Impurity scattering, Hall effect, Seebeck effect

Introduction

Zn–IV–N_2 (IV = Si, Ge, Sn) compounds, which are derived from wurtzite-type group III nitride by replacing the group III elements with an equal number of Zn and group IV elements, can be regarded as a pseudo group III nitride [1, 2]. It has been demonstrated that similar to the well-known In_xGa_xN system, the bandgap (E_g) of alloyed $ZnSn_xGe_{1-x}N_2$ was tunable from 3.1 to 2.0 eV by varying the Sn content (x) from 0 to 1 [3]. This makes Zn–IV–N_2 an intriguing semiconductor system, and studies on $ZnSn_xGe_{1-x}N_2$ as a counterpart to the $In_xGa_{1-x}N$ system have been carried out in recent years [3, 4].

Zinc tin nitride ($ZnSnN_2$) is the least studied Zn–IV–N_2 compound. For example, the synthesis of $ZnSnN_2$ thin films [5, 6] and powders [7, 8] has been reported in only the last 5 years. Since theoretical studies showed that the E_g value of 1.0–2.0 eV for $ZnSnN_2$ is appropriate for a photovoltaic absorber [1, 2, 9–11], experimental investigations have been carried out on this material [12–15]. Indeed, $ZnSnN_2$ has a large optical absorption coefficient (~ 10^5 cm^{-1}) in most of the solar spectrum [13]. In addition, p-Si/n-$ZnSnN_2$ and p-SnO/n-$ZnSnN_2$ p–n junctions for photovoltaic application were successfully fabricated recently [15, 16].

$ZnSnN_2$ has two phases that depend on the ordering of the cation sublattice: the ordered phase, which is derived by alternately replacing the cation sublattice with Zn and Sn in the wurtzite structure; the disordered-phase, in which Zn and Sn randomly occupy the cation sublattice. Theoretical studies showed that E_g of $ZnSnN_2$ is dependent on the cation-sublattice ordering: $E_g = 2$ eV for the ordered phase and $E_g = 1$ eV for the disordered phase [10, 17]. Optical studies on ordered- and disordered-$ZnSnN_2$ thin films obtained E_g values close to the above-mentioned theoretical values [10, 12, 14, 17, 18]. Owing to intensive study from theoretical and experimental points of view, the intrinsic E_g value of $ZnSnN_2$ has gradually become clear.

However, even though control of the transport properties is also important for photovoltaic applications, such properties of $ZnSnN_2$ are not well understood. $ZnSnN_2$ thin films usually show degenerate n-type conductivity owing to unintentional oxygen doping [12, 18]. The oxygen impurities occupy the nitrogen sites and behave as

*Correspondence: n-yamada@isc.chubu.ac.jp
[1] Department of Applied Chemistry, Chubu University, 1200 Matsumoto, Kasugai, Aichi 487-8501, Japan
Full list of author information is available at the end of the article

electron donors [11]. As a result, $ZnSnN_2$ films have electron densities of the order of 10^{19}–10^{21} cm^{-3} [9, 10, 12, 14, 17, 18]. The electron mobility of $ZnSnN_2$ thin films are usually 10 cm^2 V^{-1} s^{-1} or lower [9, 10, 12, 14, 17, 18] even though the films are single crystalline. To establish $ZnSnN_2$ as a photovoltaic absorber, the major challenges include suppression of the conduction electron density and enhancement of the electron mobility.

For the suppression of the conduction electron density, Floretti et al. proposed a method in which hydrogen doping takes place during film growth and subsequent annealing [19]. They successfully obtained nondegenerate $Zn_{1+\delta}Sn_{1-\delta}N_2$ films with a carrier density of 10^{16} cm^{-3}. On the other hand, no method for improving the electron mobility has been reported so far, and the low electron mobility remains one of the open questions of the electron-transport properties of $ZnSnN_2$. In the case of heavily-doped GaN epilayers with an electron density of $\sim 10^{20}$ cm^{-3} [20], an electron mobility above 100 cm^2 V^{-1} s^{-1} has been obtained. In comparison, the electron mobility of $ZnSnN_2$ appears to be unusually low, but an understanding of the limiting factor of the electron mobility in $ZnSnN_2$ is lacking.

In this study, detailed analysis of the electron-transport properties of epitaxially grown $ZnSnN_2$ thin films was carried out to elucidate the reason for the low electron mobility. Herein, we present the analysis results and discuss in detail the limiting factor of the mobility.

Results and discussion

Cation-disordered $ZnSnN_2$ films were grown on the (111) plane of yttria-stabilized zirconia (YSZ) single-crystalline substrates with a temperature of 300 °C; the films were grown by reactive radio-frequency magnetron sputtering using a Zn–Sn alloy target with Zn concentration of 50 at.%. In general, high growth temperature is preferable for the growth of thin films composed of larger crystalline grains with higher crystallinity. In the case of $ZnSnN_2$, however, the highest growth temperature is limited to ~ 300 °C, because the decomposition temperature of this compound was estimated to be ~ 350 °C [8]. Indeed, we previously confirmed that no film was grown on YSZ (111) at 350 °C [18]. Accordingly, 300 °C is the highest temperature for the growth of $ZnSnN_2$ thin films.

Out-of-plane and in-plane X-ray diffraction (XRD) measurements confirmed that the $ZnSnN_2$ films were epitaxially grown on YSZ(111) with the epitaxial relationship of $(0001)[2\bar{1}\bar{1}0]_{ZnSnN_2}$ || $(111)[\bar{1}10]_{YSZ}$ (Additional file 1: Fig. S1). The Zn/(Zn + Sn) atomic ratio in the films was determined by X-ray photoelectron spectrometry (XPS) to be in the range of 0.52–0.55. That is, slightly Zn-rich off-stoichiometric films were obtained in this study. The XPS measurements also confirmed that all the films were unintentionally doped with oxygen, forming $ZnSnN_{2-x}O_x$. The oxygen content x could be controlled by varying the nitrogen partial pressure (P_{N_2}) during the growth [18]. When P_{N_2} was decreased from 2.0 to 1.2 Pa, x in $ZnSnN_{2-x}O_x$ increased from 0.056 to 0.079 (the x values were semi-quantitatively determined by using the integrated intensity of the O 1*s* core spectra). The XPS spectra and elemental composition data are given in Additional files 2 and 3, respectively. Impurity substitution usually expand or shrink a unit cell, leading to a small shift of XRD peak. In the case of the $ZnSnN_{2-x}O_x$ films with $x < 0.08$, however, significant peak shift by the incorporation of oxygen was not observed (Additional file 4: Fig. S3a), indicating that the lattice constant did not change (Additional file 4: Fig. S3b). The difference of the ionic radii of N^{3-} (146 pm) and O^{2-} (138 pm) is so small that the oxygen substitution hardly caused the change of the lattice constant.

Hall-effect measurements were carried out to determine the carrier density (n_e) and Hall mobility (μ_H) in the films. As shown in Fig. 1a, n_e increased with increasing x, indicating that the unintentionally incorporated oxygen (O_N) served as an electron donor. Temperature (T)-independent behavior of n_e can be seen in Fig. 1b, which suggests that the $ZnSnN_{2-x}O_x$ films were degenerate semiconductors. The curve in Fig. 1a represents n_e calculated assuming that 30% of O_N was ionized (the

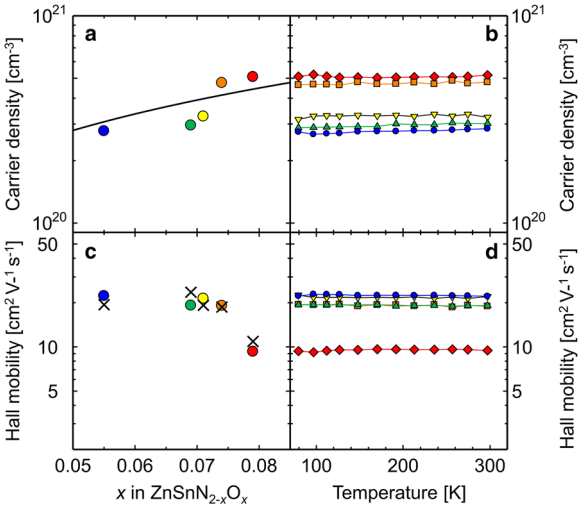

Fig. 1 **a** Electron density (n_e) and **c** Hall mobility (μ_H) at room temperature as functions of x in $ZnSnN_{2-x}O_x$ (closed circles). The solid line in **a** represents the carrier density calculated based on the assumption that the ionization rate of the incorporated oxygen was 30%. The cross marks in **c** represent the optically derived mobility (μ_{opt}). Temperature dependence of **b** n_e and **d** μ_H; the circles, triangles, inverted triangles, squares, and diamonds represent the values for films with $x = 0.055$, 0.069, 0.071 0.074, and 0.079, respectively. All the data are included in Additional file 5

ionization rate of $\eta = 30\%$). The curve reasonably approximated the experimental n_e values, indicating that O_N was highly compensated at room temperature (RT). The reason for such high compensation is probably related to the Zn-rich composition of the films. The Zn excess introduces Zn_{Sn} acceptor-like defects in $ZnSnN_2$ [19]. Recent theoretical calculation suggests that electrically neutral Zn_{Sn}–$2O_N$ complexes forms when Zn_{Sn} and O_N coexist in $ZnSnN_2$ [21]. The formation of the Zn_{Sn}–$2O_N$ complexes implies the compensation of the O_N donors. Hence, many Zn_{Sn}–$2O_N$ complexes are likely to present in the epilayers.

Figure 1c shows the x dependence of μ_H at RT. The unintentional oxygen doping caused the decrease in μ_H, suggesting that O_N acted as an impurity scattering center. Indeed, the μ_H values were independent of T (Fig. 1c), representing typical behavior of mobility limited by ionized- or neutral-impurity scattering in degenerate semiconductors. Furthermore, the T-independent behavior of μ_H clearly indicates that the contribution of T-dependent phonon scattering to electron transport was negligible.

Recently, Hamilton et al. reported that grain-boundary scattering is one of mobility-limiting factors in polycrystalline films in $ZnSnN_{2-x}O_x$ [19]. Even in epitaxial films, grain-boundary scattering sometimes cannot be ignored, because epitaxial films frequently have a biaxially-oriented grain structure [22–24]. As we previously reported, $ZnSnN_2$ epitaxial films sputtered on YSZ (111) have a compact grain structure with lateral grain diameters of ~30 nm [18]. In other words, sputtered $ZnSnN_{2-x}O_x$ epilayers are not single-crystalline films but rather biaxially-oriented polycrystalline films. Accordingly, grain-boundary scattering should be considered, when we analyze the electron transport properties of the sputtered $ZnSnN_{2-x}O_x$ epilayers. The optically derived mobility (μ_{opt}) using the Drude model corresponded to the intra-grain mobility without the grain boundary contribution, whereas DC-measured μ_H included the contribution of the grain-boundary scattering. To obtain the μ_{opt} values, we measured the infrared reflectance spectra of the $ZnSnN_{2-x}O_x$ films at near-normal incidence (~5°) in the wavelength range of 1–5 μm, and then fitting analysis was carried out using the Drude model. In our previous study, we showed that the frequency (ω)-dependent dielectric function of the $ZnSnN_{2-x}O_x$ ($\varepsilon(\omega)$) can be modeled by combining the Drude function ($\varepsilon_D(\omega)$) with double Tauc–Lorentz (TL) functions [$\varepsilon_{TL1}(\omega)$ and $\varepsilon_{TL2}(\omega)$]: i.e., $\varepsilon(\omega) = \varepsilon_{TL1}(\omega) + \varepsilon_{TL2}(\omega) + \varepsilon_D(\omega)$. The Drude function is given by

$$\varepsilon_D(\omega) = -\frac{\omega_p}{\omega^2 - i\Gamma_D\omega}, \quad (1)$$

$$\omega_p^2 = \frac{en_e}{\varepsilon_0 m^*}, \quad (2)$$

where ω_p is the plasma frequency, Γ_D is the scattering rate, ε_0 is the static dielectric constants of free space, and m^* is the effective mass. The TL function is given in Ref. [25]. The theoretical reflectance spectra calculated through the Fresnel formula combined with the modeled dielectric function were fitted to the experimental spectra (ω_p and Γ_D were used as the fitting parameters). In the fitting analysis, the parameters in the TL functions were fixed for simplicity at constant values that were the same as reported values in the literature [13]. We obtained good fits, as shown in Fig. 2a–d. The best-fit parameters are listed in Additional file 7: Table S2 (Additional file 7). Using the best-fit parameters, the μ_{opt} values were calculated using the relationship

$$\mu_{opt} = \frac{1}{en_e}\frac{\varepsilon_0\omega_p^2}{\Gamma_D}. \quad (3)$$

The values of μ_{opt} and μ_H were almost identical, as shown in Fig. 1c, indicating that the contribution of grain-boundary scattering to the electron transport in the $ZnSnN_{2-x}O_x$ epilayers was negligible. In other words, μ_H corresponded to the intra-grain mobility, implying that the electron transport properties of the $ZnSnN_{2-x}O_x$ epilayers were close to those of single crystalline films.

Here, we compare μ_H values of the $ZnSnN_{2-x}O_x$ epilayers with those of InN epilayers. Figure 3 shows n_e versus μ_H plot for the $ZnSnN_{2-x}O_x$ and InN epilayers [26, 27]. The μ_H values of the present $ZnSnN_{2-x}O_x$ films are in comparable level with those of the degenerate InN epilayers reported in the 1990s. Nevertheless, the μ_H values in the present study are substantially lower than those of the

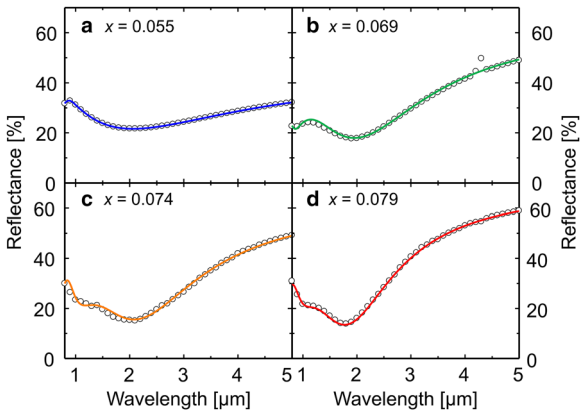

Fig. 2 Infrared reflectance spectra of $ZnSnN_{2-x}O_x$ epilayers with $x =$ **a** 0.055, **b** 0.069, **c** 0.074, and **d** 0.079. The results of least-squares fitting using the modeled dielectric function are represented by solid lines. All the data are included in Additional file 6

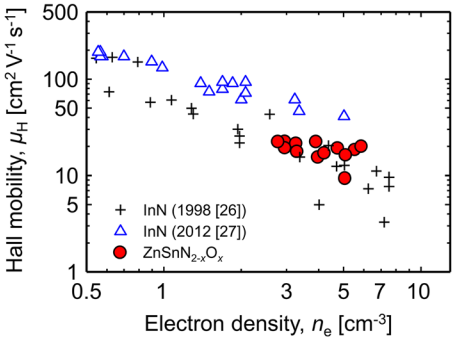

Fig. 3 Comparison of Hall mobility (μ_H) as a function of electron density (n_e) for $ZnSnN_{2-x}O_x$ and degenerate InN epilayers [26, 27]. All the data are included in Additional file 8

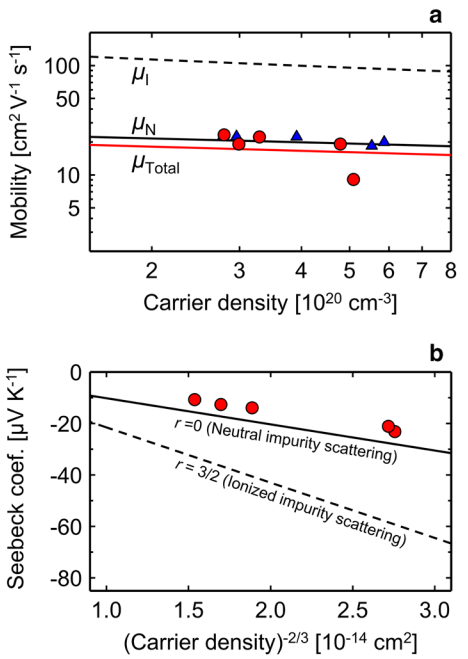

Fig. 4 **a** Dependence of Hall mobility on carried density. The circles represent data for the same films shown in Figs. 1 and 2. The triangles represent data for films grown under conditions similar to those employed for the grown of films shown in Figs. 1 and 2. The lines labeled μ_I and μ_N are theoretical curves of mobility limited by ionized- and neutral-impurity scatterings, respectively. The curve labeled μ_{total} represents the total mobility calculated from $\mu_{total} = (1/\mu_I + 1/\mu_N)^{-1}$. **b** Seebeck coefficient as a function of (carrier density)$^{-2/3}$; theoretical lines for $r = 3/2$ (dashed line) and 0 (solid line) are also included. All the data are included in Additional file 9

InN layers fabricated in 2010s. We believe that there is still room for the improvement of electron mobility, if the mobility-limiting factors are fully understood.

To obtain insight into the intra-grain electron transport in $ZnSnN_{2-x}O_x$, the μ_H values were compared with theoretical models. We first considered ionized-impurity scattering, which generally governs the electron transport in heavily-doped degenerate semiconductors. The theoretical mobilities limited by the ionized-impurity scattering (μ_I) were calculated by using the Brooks–Herring model [28]. We used an effective mass of $0.37m_0$ [18] and a static dielectric constant (ε_s) of 11[1] for the calculation. The calculated μ_I is plotted as a function of n_e in Fig. 4a. The μ_I curve gives the upper limit of the electron mobility in $ZnSnN_{2-x}O_x$; namely, the electron mobility of $ZnSnN_{2-x}O_x$ potentially reaches ~100 cm^2 V^{-1} s^{-1}. Nevertheless, the experimental μ_H values had a maximum of 20 cm^2 V^{-1} s^{-1}, implying that an additional scattering source must be taken into account.

Thermopower measurements were carried out for further investigation. For highly degenerate *n*-type semiconductors with a parabolic conduction band, Seebeck coefficient (*S*) is given by [28]

$$S = -\frac{8\pi^2}{3}\left(r+\frac{3}{2}\right)\frac{k_B^2 m^* T}{eh^2} n_e^{-\frac{2}{3}}, \quad (4)$$

where *r* represents the scattering constant (e.g., $r = 3/2$ for ionized-impurity scattering, and $r = 0$ for neutral-impurity scattering), k_B is the Boltzmann constant, and *h* is the Planck constant. A plot of *S* versus $n_e^{-2/3}$ allows us to gain insight into the electron-transport mechanisms from the viewpoint of *r* values [29]. As shown in Fig. 4b, the experimental data lie close to the theoretical curve for $r = 0$ (solid line), whereas the experimental *S* values are located away from the theoretical *S* curve (dashed line) for the ionized-impurity scattering ($r = 3/2$). These trends suggest that neutral-impurity scattering was the dominant scattering mechanism. The temperature-independent behavior of μ_H is consistent with this interpretation because neutral-impurity scattering does not depend on temperature [30, 31]. Since ~70% of O_N was not ionized (Fig. 1a), it is reasonable to suppose that the compensated oxygen that is likely to form the Zn_{Sn}–$2O_N$ complex acted as the neutral-impurity scattering centers. In fact, Hamilton et al. recently pointed out the possibility that the Zn_{Sn}–$2O_N$ complexes behave as the neutral-impurity scattering centers [21].

We further analyzed the n_e–μ_H data by taking account of the neutral-impurity scattering. We hypothesized that all the compensated oxygen served as neutral-impurity scattering centers, namely, the density of the neutral impurity (n_N) was defined as $n_N = (n_e/\eta)(1-\eta)$. The mobility limited by the neutral-impurity scattering (μ_N) was calculated on the basis of the model developed by Mayer et al. [31]:

$$\mu_N = \frac{e^3 m^*}{4\pi\varepsilon_s\varepsilon_0 A(w)\hbar^3}\frac{1}{n_N}, \quad (5)$$

where $w=(k_F a_B)^2$,

$$A(w) = \frac{35.2}{w^{\frac{1}{2}}}\frac{\left(1+e^{-50w}\right)\left(1+80.6w+23.7w^2\right)}{1+41.3w+133w^2}\left[\frac{1}{w}\ln(1+w) - \frac{1+\frac{1}{2}w-\frac{1}{6}w^2}{(1+w)^3}\right], \quad (6)$$

k_F is the Fermi wave number, and a_B is the effective Bohr radius ($a_B=1.5$ nm for $ZnSnN_2$). Assuming that the ionization ratio of O_N was $\eta=30\%$, the total mobility was calculated using Matthiessen's rule, $\mu_{Total}=(1/\mu_N+1/\mu_I)^{-1}$. The calculated n_e–μ_{total} curve agrees well with the experimental n_e–μ_H data, as shown in Fig. 4a. Furthermore, we grew an additional series of $ZnSnN_{2-x}O_x$ epilayers under conditions similar to those mentioned above, and their n_e–μ_H data are also plotted in Fig. 4a (triangles). Again, the experimental data was found to be located near the theoretical n_e–μ_{total} curve. These findings led us to the conclusion that the unintentionally incorporated oxygen had an ionization rate as low as approximately ~30% and the unionized oxygen acted as neutral-impurity scattering centers that dominated electron transport in the heavily-doped $ZnSnN_{2-x}O_x$ epitaxial films. The low μ_H values in the $ZnSnN_{2-x}O_x$ epilayers resulted from the high concentration of neutral oxygen impurities. Frequently reported low electron mobilities in $ZnSnN_2$ epitaxial films can be explained by the same reason. Recent study showed that μ_H of $ZnSnN_{2-x}O_x$ films with very high oxygen contents ($x>0.4$) was as low as <5 cm^2 V^{-1} s^{-1} [21]. That is, the more the oxygen content increases, the lower μ_H becomes. This supports the idea that electron scattering by the oxygen-related defects governs the electron-transport properties of $ZnSnN_{2-x}O_x$.

Conclusions

In summary, we analyzed the electron-transport properties of unintentionally oxygen-doped $ZnSnN_2$ epitaxial layers. We confirmed that the incorporated oxygen impurities behaved as electron donors with the low ionization rate of 30%. The Hall- and Seebeck-effect measurements revealed that the compensated oxygen impurities, which are likely to form the electrically neutral Zn_{Sn}–$2O_N$ complexes, behaved as neutral-impurity scattering centers and further governed electron transport in the $ZnSnN_{2-x}O_x$. The low ionization rate led to the high concentration of neutral-impurity scattering centers. Therefore, we conclude that the low electron mobilities reported even in $ZnSnN_2$ single-crystalline films are attributed to the high concentration of neutral oxygen impurities. Suppression of the oxygen concentration in $ZnSnN_2$ is crucial not only to obtain nondegenerate $ZnSnN_2$, but also to achieve high mobility.

Methods

Thin-film growth

Reactive radio-frequency (RF) magnetron sputtering was employed to grow $ZnSnN_2$ epitaxial films on YSZ(111) single-crystalline substrates at the growth temperature of 300 °C. The base pressure of $\sim 2\times10^{-4}$ Pa was established prior to the film-growth. A disk of $Zn_{0.5}Sn_{0.5}$ alloy was used as a target (diameter of 10 cm and purity of 3 N). An RF power of 70 W was applied to the target. A mixture of Ar and N_2 gas with various $N_2/(N_2+Ar) \equiv f(N_2)$ ratios was introduced into the chamber through two independent mass flow controllers with a total flow rate of 5 sccm. The total pressure in the growth chamber (P) was held at 2.0 Pa during film growth. The nitrogen partial pressure was defined as $P_{N2}=f(N_2)\times P$. The growth time was adjusted to obtain films with thicknesses of 100–300 nm. Prior to the film growth, a 5 min-long sputter-etching with pure Ar gas was performed, followed by a 5 min-long pre-sputtering under the same condition with the film growth. After the film growth, the as-grown films were immediately stored in another vacuum chamber (the pressure was about 1 Pa) for subsequent measurements.

Characterization

A Rigaku ATX-G X-ray diffractometer with Cu Kα radiation was employed to perform out-of-plane (θ/ω) and in-plane ($2\theta_\chi/\phi$) scans to confirm the epitaxial growth. The compositions (Zn/(Zn + Sn) and x) of the $ZnSnN_2$ films were examined by XPS (PHI Versa Probe), using monochromated Al Kα ($h\nu=1486.6$ eV) radiation. The XPS measurements were performed on 3-min Ar^+-sputter-etched surface of the films. The relative sensitivity factor (RSF) approach was exploited to determine the compositions. It was confirmed that the compositions determined by the RSF method were consistent with those determined by Rutherford backscattering spectrometry [29, 32]. Hence, we believe that the compositions in this study are sufficiently reliable. The details of the RSF approach were already described elsewhere [18]. Electrical properties were determined by Hall-effect measurements in the van der Pauw configuration (Toyo Corp. Resitest 8200). Optical transmittance and reflectance were collected between 0.3 and 5.0 μm using a UV–Vis-NIR spectrophotometer (Shimadzu UV-3150) and FTIR spectrometer (Shimadzu IRAffinity-1).

Fitting analysis of reflectance spectra

As seen from Fig. 2a–d, free-electron reflection is clearly seen in the IR region. The well-known Drude dielectric

model (Eqs. 1, 2) was employed to describe the optical response by the free electrons. In addition to the Drude model, the Tauc–Lorentz (TL) dispersion model was considered to describe the optical response across the whole spectral region. The explicit expression of the TL model is given in literature [25]. Deng et al. previously demonstrated that the dielectric response of $ZnSnN_2$ in the UV to visible region can be reproduced by double TL functions [13]. Hence, we modelled the dielectric function of degenerate $ZnSnN_{2-x}O_x$ as a sum of double TL and Drude functions. Theoretical reflectance spectra calculated via the Fresnel formulas combined with the dielectric function above were fitted to the experimental spectra. In the fitting analysis, the parameters in the TL functions were fixed for simplicity at constant values that were the same as the values reported by Deng et al. [13]. Thus, ω_p and Γ_D in the Drude function were used as the fitting parameters.

Additional files

Additional file 1. Typical out-of-plane and in-plane XRD patterns for $ZnSnN_2$ epitaxial films grown on YSZ (111).

Additional file 2. Oxygen 1s core spectra of $ZnSnN_2$ unintentionally doped with oxygen.

Additional file 3. Zn/(Zn + Sn) atomic ratio and *x* in $ZnSnN_{2-x}O_x$.

Additional file 4. Out-of-plane XRD patterns for $ZnSnN_{2-x}O_x$ films with different *x* values and *x*-dependence of *c*-axis length.

Additional file 5. Electron density and mobility as functions of temperature and oxygen impurity concentration, *x*.

Additional file 6. Experimental reflectance and the best-fit curves using the TL and Drude combination model.

Additional file 7. Electron density and Drude parameters (plasma frequency, ω_p and broadening factor, Γ_D in the Drude function) extracted from the best-fit spectra shown in Fig. 2a—e in the main text.

Additional file 8. n_e vs. μ_H data for $ZnSnN_{2-x}O_x$ and InN epilayers. The data for InN were taken from Refs. [26, 27].

Additional file 9. Theoretical mobility (n_e vs. μ) and n_e vs. *S* data shown in Fig. 4.

Abbreviations

μ_H: Hall mobility; n_e: electron density; O_N: impurity oxygen on nitrogen site in $ZnSnN_2$; *x*: oxygen content in $ZnSnN_{2-x}O_x$; XPS: X-ray photoelectron spectroscopy; XRD: X-ray diffraction; Zn_{Sn}: zinc atom on tin site in $ZnSnN_2$.

Acknowledgements

The authors acknowledge M. Kawamura (Institute of Science and Technology Research, Chubu University) for providing useful advice on XRD and XPS measurements.

Author contributions

NY and FK designed the experiments. XC performed fabrication and measurements. NY carried out the theoretical analysis. TT, YN and NY were the PIs. XC and NY wrote the manuscript. All authors discussed the results and reviewed the manuscript. All authors read and approved the final manuscript.

Funding

This work was supported by Japan Society for the Promotion of Science (JSPS) KAKENHI (Grant No. 16H04500). The funder had no role in study design, data collection and analysis, decision to publish, or preparation of the manuscript.

Availability of data and materials

All data generated or analyzed during this study are included in Additional files 1–9.

Competing interests

The authors declare that they have no competing interests.

Author details

[1] Department of Applied Chemistry, Chubu University, 1200 Matsumoto, Kasugai, Aichi 487-8501, Japan. [2] High Pressure Group, National Institute for Materials Science (NIMS), 1-1 Namiki, Tsukuba, Ibaraki 305-0044, Japan.

Received: 9 October 2019 Accepted: 12 January 2020
Published online: 27 February 2020

References

1. Paudel TR, Lambrecht WRL. First-principles study of phonons and related ground-state properties and spectra in Zn–IV–N_2 compounds. Phys Rev B. 2008;78:115204.
2. Punya A, Lambrecht WRL, Schilfgaarde M. Quasiparticle band structure of Zn–IV–N_2 compounds. Phys Rev B. 2011;84:165204.
3. Narang P, Chen S, Coronel NC, Gul S, Yano J, Wang LW, Lewis NS, Atwater HA. Bandgap tunability in Zn(Sn, Ge)N_2 semiconductor alloys. Adv Mater. 2014;26:1235–41.
4. Shing AM, Coronel NC, Lewis NS, Atwater HA. Semiconducting $ZnSn_xGe_{1-x}N_2$ alloys prepared by reactive radio-frequency sputtering. APL Mater. 2015;3:76104.
5. Coronel NC, Lahourcade L, Delaney KT, Shing AM, Atwater HA. Earth-abundant $ZnSn_xGe_{1-x}N_2$ alloys as potential photovoltaic absorber materials. In: Proceedings of the 38th IEEE photovoltaic specialists conference. New York: IEEE; 2012. p. 3204–7.
6. Feldberg N, Keen B, Aldous JD, Scanlon DO, Stampe PA, Kennedy RJ, Reeves RJ, Veal TD, Durbin SM. $ZnSnN_2$: a new earth-abundant element semiconductor for solar cells. In: Proceedings of the 38th IEEE photovoltaic specialists conference. New York: IEEE; 2012. p. 2524–7
7. Quayle PC, He K, Shan J, Kash K. Synthesis, lattice structure, and band gap of $ZnSnN_2$. MRS Commun. 2013;3:135–8.
8. Kawamura F, Yamada N, Imai M, Taniguchi T. Synthesis of $ZnSnN_2$ crystals via a high-pressure metathesis reaction. Cryst Res Technol. 2016;51:220–4.
9. Lahourcade L, Coronel NC, Delaney KT, Shukla SK, Spaldin NA, Atwater HA. Structural and optoelectronic characterization of RF sputtered $ZnSnN_2$. Adv Mater. 2013;25:2562–6.
10. Feldberg N, Aldous JD, Linhart WM, Phillips LJ, Durose K, Stampe PA, Kennedy RJ, Scanlon DO, Vardar G, Field RL, Jen TY, Goldman RS, Veal TD, Durbin SM. Growth, disorder, and physical properties of $ZnSnN_2$. Appl Phys Lett. 2013;103:42109.
11. Chen S, Narang P, Atwater HA, Wang LW. Phase stability and defect physics of a ternary $ZnSnN_2$ semiconductor: first principles insights. Adv Mater. 2014;26:311–5.
12. Fioretti AN, Zakutayev A, Moutinho H, Melamed C, Perkins JD, Norman AG, Al-Jassim M, Toberer ES, Tamboli AC. Combinatorial insights into doping control and transport properties of zinc tin nitride. J Mater Chem C. 2015;3:11017.
13. Deng F, Cao H, Liang L, Li J, Gao J, Zhang H, Qin R, Liu C. Determination of the basic optical parameters of $ZnSnN_2$. Opt Lett. 2015;40:1282–5.
14. Martinez AD, Fioretti AN, Toberer E, Tamboli AC. Synthesis, structure, and optoelectronic properties of II–IV–V2 materials. J Mater Chem A. 2017;5:11418.
15. Qin R, Cao H, Liang L, Xie Y, Zhuge F, Zhang H, Gao J, Javaid K, Liu C, Sun W. Semiconducting $ZnSnN_2$ thin films for Si/$ZnSnN_2$ *p–n* junctions. Appl Phys Lett. 2016;108:142104.

16. Javaid K, Yu J, Wu W, Wang J, Zhang H, Gao J, Zhuge F, Liang L, Cao H. Thin film solar cell based on $ZnSnN_2$/SnO heterojunction. Phys Status Solidi PRL. 2018;12:1700332.
17. Veal TD, Feldberg N, Quackenbush NF, Linhart WM, Scanlon DO, Piper LFJ, Durbin SM. Band gap dependence on cation disorder in $ZnSnN_2$ solar absorber. Adv Energy Mater. 2015;5:1501462.
18. Cao X, Kawamura F, Ninomiya Y, Taniguchi T, Yamada N. Conduction-band effective mass and bandgap of $ZnSnN_2$ earth-abundant solar absorber. Sci Rep. 2017;7:14987.
19. Fioretti AN, Stokes A, Young MR, Gorman B, Toberer ES, Tamboli AC, Zakutayev A. Effects of hydrogen on acceptor activation in ternary nitride semiconductors. Adv Electron Mater. 2017;3:1600544.
20. Gaskill DK, Rowland LB, Doverspike K. Electrical transport properties of AlN, GaN and AlGaN. In: Edger JH, editor. Properties of group III nitrides, EMIS Data Reviews Series No. 11. London: Inspec; 1994. p. 105.
21. Hamilton DC, Arca E, Pan J, Siol S, Young M, Lany S, Zakutayev A. Electron scattering mechanisms in polycrystalline sputtered zinc tin oxynitride thin films. J Appl Phys. 2019;126:035701.
22. Yan M, Lane M, Kannewurf CR, Chang PH. Highly conductive epitaxial CdO thin films prepared by pulsed laser deposition. Appl Phys Lett. 2001;78:2342–4.
23. Furubayashi Y, Yamada N, Hirose Y, Yamamoto Y, Otani M, Hitosugi T, Shimada T, Hasegawa T. Transport properties of *d*-electron based transparent conducting oxide: anatase $Ti_{1-x}Nb_xO_2$. J Appl Phys. 2007;101:093705.
24. Zhu QY, Ye ZZ, Yuan GD, Huang JY, Zhu LP, Zhao BH, Lu JG. Synthesis and characterization of Al–N codoped p-type ZnO epitaxial films using high-temperature homo-buffer layer. Appl Surf Sci. 2006;253:1903–6.
25. Jellison GE Jr, Modine FA. Parameterization of the optical functions of amorphous materials in the interband region. Appl Phys Lett. 1996;69:371–3.
26. Yamamoto A, Shin-ya T, Sugiura T, Hashimoto A. Characterization of MOVPE-grown InN layers on α-Al_2O_3 and GaAs substrates. J Cryst Growth. 1998;189–190:461–5.
27. Rauch C, Tumisto F, King PDC, Veal TD, Lu H, Schaff WJ. Self-compensation in highly n-type InN. Appl Phys Lett. 2012;101:011903.
28. Seeger K. Semiconductor physics; an introduction. New York: Springer; 2011.
29. Cao X, Yamaguchi Y, Ninomiya Y, Yamada N. Comparative study of electron transport mechanisms in epitaxial and polycrystalline zinc nitride films. J Appl Phys. 2016;119:025104.
30. Erginsoy C. Neutral impurity scattering in semiconductors. Phys Rev. 1950;79:1013–4.
31. Meyer JR, Bartoli FJ. Phase-shift calculation of electron mobility in n-type silicon at low temperatures. Phys Rev B. 1981;24:2089–100.
32. Núñez CG, Pau JL, Hernández MJ, Cervera M, Ruiz E, Piqueras J. On the zinc nitride properties and the unintentional incorporation of oxygen. Thin Solid Films. 2012;520:1924–9.

Publisher's Note